

Active Nuclei and Star-Forming Objects at  $z > 2$ :  
Metallicities, Winds, and Formation Histories

William C. Keel – University of Alabama

Wentao Wu – University of Alabama

Ian Waddington – Arizona State University

Rogier A. Windhorst – Arizona State University

Sebastian M. Pascarelle – Arizona State University

Deposited 09/18/2018

Citation of published version:

Keel, W., Wu, W., Waddington, I., Windhorst, R., Pascarelle, S. (2002): Active Nuclei and Star-Forming Objects at  $z > 2$ :Metallicities, Winds, and Formation Histories. *The Astronomical Journal*, 123(6). DOI: [10.1086/340696](https://doi.org/10.1086/340696)

## ACTIVE NUCLEI AND STAR-FORMING OBJECTS AT $z > 2$ : METALLICITIES, WINDS, AND FORMATION HISTORIES<sup>1</sup>

WILLIAM C. KEEL<sup>2</sup> AND WENTAO WU<sup>3</sup>

Department of Physics and Astronomy, University of Alabama, Box 870324, Tuscaloosa, AL 35487

AND

IAN WADDINGTON,<sup>4</sup> ROGIER A. WINDHORST, AND SEBASTIAN M. PASCARELLE<sup>2,5</sup>  
Department of Physics and Astronomy, Arizona State University, Box 1504, Tempe, AZ 85287-1504

Received 2002 February 4; accepted 2002 March 12

### ABSTRACT

We present near-infrared observations of the active galactic nuclei (AGNs) and star-forming objects in the field of the radio galaxy 53W002 at  $z = 2.39$ . The star-forming objects are of special interest as candidate protogalactic objects. The 1.1–2.2  $\mu\text{m}$  passbands sample the emitted-optical range at this redshift, providing new diagnostics of the structure, metal abundance, and age of the members of this grouping originally selected through Ly $\alpha$  emission. The star-forming objects are uniformly very blue in continuum slope, which fits with the strong Ly $\alpha$  emission in indicating metal abundances that are less than half solar; some are as blue as the most metal-poor local objects. They fall in a range of luminosity and metallicity that is not populated by local objects, indicating a shorter star-forming history at this early epoch. The best local analogs, such as Mrk 66 and 357, either have several times lower luminosity at comparable [O/H] or significantly higher [O/H] for comparable luminosity. Spectroscopy from the Near-Infrared Camera and Multi-Object Spectrometer yields detections of [O III] emission for two objects and interesting [O III] and H $\beta$  limits for the rest, augmented by H $\alpha$  limits from Infrared Telescope Facility imaging. These data are satisfied by model stellar populations that have been forming stars for the last  $2\text{--}5 \times 10^6$  yr before  $z = 2.39$ . We do not see evidence for older pre-existing stellar populations, either in the broadband colors or as redder halos in which the star-forming regions are imbedded. These results suggest that the compact star-forming objects we see at  $z = 2.0\text{--}2.5$  are indeed early stages in the building of galaxies rather than transient star-forming events in larger pre-existing dynamical systems. The results also allow an alternative scheme, in which these are low-mass systems that are blowing winds rather than self-enriching, in which case they should fade rapidly with cosmic epoch. For the three prominent AGNs at  $z = 2.39$ , H $\alpha$  and [O III] emission were measured. Unlike the fainter star-forming objects, their line ratios (specifically Ly $\alpha$ /H $\alpha$ ) show metallicities just as high as in nearby systems. If the AGNs occur in those systems that started with the highest density and began active star formation before the less massive surrounding objects, they will have higher metallicity (as we see in their emitted-ultraviolet line ratios). The “ionization cones” seen prominently in Ly $\alpha$  also appear in [O III] and H $\alpha$ , with a role for continuum reflection in some cases as well. The contrast between the AGNs and fainter star-forming objects can be broadly accommodated in a hierarchical formation picture, although there are still important unknowns as to the fate of the star-forming objects.

*Key words:* galaxies: abundances — galaxies: active — galaxies: evolution

### 1. INTRODUCTION

Our view of galaxies is being revolutionized by the opening of galaxy evolution to direct observational study. Systematic changes in the integrated star formation rate with redshift are well attested, although the details of these changes are still under debate (Madau et al. 1996; Madau, Pozzetti, & Dickinson 1998; Pascarelle, Lanzetta, & Fernandez-Soto 1998a; Haarsma et al. 2000; Thompson, Wey-

mann, & Storrie-Lombardi 2001; Lanzetta et al. 2002), and changes in the galaxy content of rich clusters give the strongest evidence for evolution among galaxies. As we move beyond this, the obvious next goal is watching galaxy formation or perhaps, more accurately, a longer process of galaxy building, which has repeatedly proven more elusive as we reach outward in redshift. Among the best candidates for protogalactic objects, especially if hierarchical CDM-like schemes apply, are the numerous faint, blue, and compact objects seen at large redshifts. A group or cluster of these was reported at  $z = 2.4$  by Pascarelle et al. (1996, hereafter P96), and similar systems prove to be common in the Hubble Deep Fields (Mobasher et al. 1996; Marleau & Simard 1998; Gardner & Satyapal 2000). These objects are of special interest as an early phase in galaxy development for several reasons. Their high emitted-ultraviolet luminosities imply correspondingly high star formation rates, but they have no obvious population of counterparts in the local universe (P96; Pascarelle, Windhorst, & Keel 1998b, hereafter P98). Most distinguishing, they are small, with effective

<sup>1</sup> Based on observations with the NASA/ESA *Hubble Space Telescope* obtained at the Space Telescope Science Institute, which is operated by the Association of Universities for Research in Astronomy, Inc., under NASA contract NAS 5-26555.

<sup>2</sup> Visiting Astronomer, NASA Infrared Telescope Facility, Mauna Kea, HI.

<sup>3</sup> Current address: Department of Physics and Astronomy, Louisiana State University, Baton Rouge, LA 70803.

<sup>4</sup> Current address: Department of Physics, H. H. Wills Physics Laboratory, University of Bristol, Tyndall Avenue, Bristol BS8 1TL, UK.

<sup>5</sup> Current address: 5004 Southern Star Terrace, Columbia, MD 21044.

radii barely resolved using the *Hubble Space Telescope* (*HST*) at redshifts  $z > 2$ , where  $0''.1$  translates to 0.5–1.0 kpc for currently popular cosmologies. There is weak evidence that the radial profiles are better fit by an  $R^{1/4}$  bulge-like form than by an exponential disk (P96), although composite structures are certainly allowed. A significant fraction of these objects are closely paired with merging timescales (incorporating pairwise velocity differences 200–300 km s<sup>-1</sup>), suggesting that they undergo rapid merging into more massive systems or indeed represent pieces of larger dynamical systems (Colley et al. 1997). They are often strong Ly $\alpha$  emitters without the additional emission lines that are strong in active galactic nuclei (AGNs), supporting an interpretation as star-forming systems. These properties are all consistent with the idea that these objects are showing us one of the final phases in galaxy formation, as star-forming protogalaxies or young galaxies grow via hierarchical merging. Their physical nature has elicited diverse opinions (Colley et al. 1996), hinging on whether they are actually seen early in the process of gas-to-star conversion or might be localized starbursts within substantially larger and relatively old systems, whose surroundings are inconspicuous because of the severe cosmological surface brightness dimming and the ultraviolet bias toward hot stars. Observations over a wider wavelength range are important in resolving this issue.

The 53W002 grouping offers an especially attractive opportunity to study several of these “subgalactic” objects in the same field, as well as AGNs of various flavors. Two of the star-forming objects in our region of interest, objects 5 and 12, turn out to be at  $z = 2.05$  (Pascarelle et al. 2002), which places their Ly $\alpha$  so near the edge of the *HST* F410M passband that we may have detected them through luck as much as statistics. We include these object in our study since their luminosities and sizes are similar to those of the star-forming objects at  $z = 2.4$ . The results of the full spectroscopic follow-up were not known when the Near-Infrared Camera and Multi-Object Spectrometer (NICMOS) observations were specified, so we pointed to include some objects (since found to be stars with excesses in the F410M passband) that we would have replaced by others in hindsight.

We present here a near-infrared study of the region surrounding 53W002, using *HST* NICMOS and Infrared Telescope Facility (IRTF) data. This wavelength regime shows us the emitted-optical range at this redshift, so we expect to see stars cooler than the B-type stars that dominate the emitted-ultraviolet range originally used to find these objects. The full spectral shape from 1100–6600 Å in the emitted frame gives a much more sensitive way to see how old the stellar populations are and provide evidence of internal extinction, while spectroscopy in the near-IR can also indicate the gas abundances from [O III] and Balmer emission. The Ly $\alpha$ /H $\alpha$  ratio can tell us, albeit in a complicated way, about the abundances and geometry in the gas and dust. For the three luminous AGNs in this sample, we can compare any host galaxy properties we can measure and examine their extended ionized gas to see how well an ionization-cone model (as suggested by the Ly $\alpha$  structures) explains them. We analyze *HST* NICMOS images and grism spectroscopy and IRTF imaging in the *K* band and redshifted H $\alpha$  to refine our understanding of how old and how large these putative young galaxies really are.

## 2. OBSERVATIONS

### 2.1. NICMOS Imaging and Spectroscopy

Two overlapping fields in the 53W002 region were observed with NICMOS, using the widest-field NIC3 camera during the first NICMOS refocus campaign in 1998 January. Direct images of 2439 s duration were obtained in the F110W and F160W filters (corresponding roughly to emitted central wavelengths 3200 and 4700 Å at  $z = 2.4$ ), along with a similar exposure in F175W (emitted-wavelength 5100 Å) to support the grism spectroscopy, although the thermal background in this passband is substantially higher than in F160W and its signal-to-noise ratio correspondingly worse. A single image set in F240M was also obtained, but the actual thermal performance of the telescope meant that only the few brightest objects in the field were detected.

We also obtained slitless spectroscopy with the NICMOS G141 grism for these two fields, with a total exposure time of 8054 s for each field. The dispersion was fortuitously oriented nearly north-south, perpendicular to the extended emission-line structure of 53W002, giving us a good spatial trace of [O III]  $\lambda$ 5007 in its ionization cones.

To complement these data for 53W002 itself, we obtained a single-orbit exposure at higher resolution using the NIC2 camera and F160W filter. The radio core jet or small double structure of 53W002 makes it the best candidate for a dynamically relaxed, perhaps young elliptical galaxy in this grouping (Windhorst, Keel, & Pascarelle 1998), so we use these data to look for any redder, extended de Vaucouleurs profile, as well as the role of line emission as evaluated with the help of the grism spectrum. At  $z = 2.39$ , [O III]  $\lambda$ 5007 is observed at 1.697  $\mu$ m, so the two [O III] lines are strong contributors in the F160W passband.

The two NICMOS fields are outlined in Figure 1 on a Wide Field Planetary Camera 2 (WFPC2) *I*-band (F814W) image showing the spectroscopically confirmed high-redshift objects, augmented with a ground-based *V* image (Keel et al. 1999) to fill in regions outside the WFPC2 footprint. The NICMOS fields include all three of the AGNs found in P96, as well as six of the fainter Ly $\alpha$  emitters (not all of which were detected in the NICMOS images). Objects 10 and 13 of P96 have since proven to be stars (Pascarelle et al. 2002), which we suspected originally given their red colors, so they are not counted henceforth. For reference, Table 1 lists the targeted objects and their spectroscopic redshifts, including Ly $\alpha$  results from Keck multislit observations presented by Pascarelle et al. (2002). The redshift of object 1 is ambiguous, with their paper listing  $z = 3.05$  as a possible redshift based on a marginal emission feature at 4955 Å. We also consider its properties if it in fact lies at  $z = 2.4$ , in which case its actual line emission would be weaker and unseen in their spectrum.

We processed the NICMOS images to remove the variable “pedestal” effect, which is a change in the bias level between the quadrants of the detector. Our fields are sparse enough that blank sky could be used to assess the offsets quite accurately, which was done by simultaneously minimizing flat-field residuals in blank-sky regions and requiring continuity of the mean sky level across the four quadrant seams. Standard STScI/NICMOS library flat fields were used. Each final image is the clipped mean of a  $3 \times 3$  dither pattern with spacing  $1''.67$  (8.3 pixels)

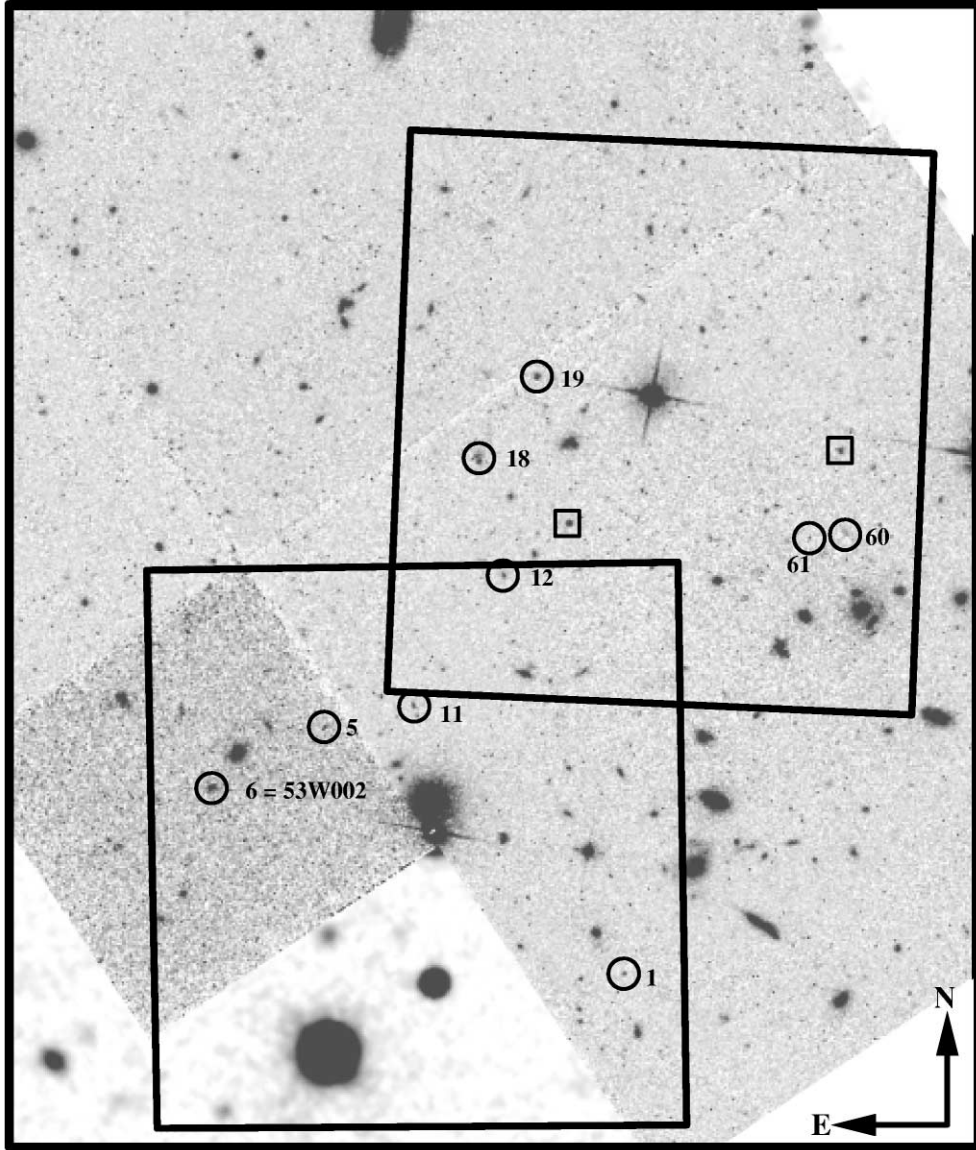


FIG. 1.—*HST* WFPC2 *I*-band (F814W) image of the 53W002 grouping, rotated to put north along the  $+y$ -axis and supplemented with a ground-based image in the area outside the WFPC2 coverage, with the fields of the NIC3 observations marked. Numbered objects have been confirmed to have Ly $\alpha$  emission at  $2.04 < z < 2.5$ , except for object 1 whose line identification is tentative. Objects 6, 18, and 19 are spectroscopically classified AGNs (object 6 is the radio galaxy 53W002 itself). Two of the candidates from Pascarelle et al. (1996, their objects 10 and 13) within the NICMOS fields have since been found to be stars, marked here with surrounding squares. The field shown spans  $94'' \times 111''$ . The deepest Ly $\alpha$  search includes the WFPC2 field but not the area outside it.

TABLE 1  
CANDIDATE OBJECTS AND REDSHIFTS

P96 ID	$\alpha$ (J2000.0)	$\delta$ (J2000.0)	Other IDs	$z$	Notes
6.....	17 14 14.74	+50 15 28.9	53W002	2.390	
18.....	17 14 11.89	+50 16 00.5	AGN	2.393	Detached companion at $z = 2.406$
19.....	17 14 11.27	+50 16 08.7	AGN	2.397	
12.....	17 14 11.66	+50 15 49.3	...	2.053	Double?
11.....	17 14 12.63	+50 15 36.8	...	2.451	Double
5.....	17 14 13.54	+50 15 34.7	...	2.048	Double?
60.....	17 14 08.16	+50 15 52.8	...	2.30:	
61.....	17 14 08.53	+50 15 52.2	...	Unknown	
1.....	17 14 10.53	+50 15 09.8	...	3.1:	
10.....	17 14 08.17	+50 16 01.4	Star	...	
13.....	17 14 10.98	+50 15 54.3	Star	...	

NOTE.—Units of right ascension are hours, minutes, and seconds, and units of declination are degrees, arcminutes, and arcseconds.

done in three successive strips of three exposures each to allow an exact match between coordinate systems in direct and grism images while retaining fine control over execution time. Pipeline removal of cosmic-ray events from the MULTIACCUM readout sequences was very effective, so that no further cosmic-ray treatment was required.

Close inspection shows ghost images 8 pixels along the detector  $+x$ -axis from the three bright stars in the NIC3 fields. These are apparently image persistence artifacts, as propagated through mosaicking with the 8 pixel dither step between successive observation sequences. None falls in a particularly damaging location for our purposes. In the grism images, there are several “zero order” images of bright objects in and beyond the southern part of each field observed, which could potentially be confused with genuine (high-redshift) emission-line objects.

The dither sequence, on a set of  $(\text{integer} + \frac{1}{3})$  pixel centers, allowed drizzle reconstruction to improve sampling. We produced a set of F110W and F160W drizzled images on a  $0''.10$  grid and show the F160W images in Figure 2. Photometry was carried out both using SExtractor to estimate total fluxes and by explicit aperture photometry with curve-of-growth corrections based on the point-spread function (PSF). Comparison shows that these almost always agree at better than the 15% level, with a few larger discrepancies traced to resolved structures such as the extended emission-line regions around the AGNs (which are prominent in F160W because of  $[\text{O III}]$  emission appearing at  $1.70 \mu\text{m}$ ). This dispersion due to image structure is larger than the purely statistical error in the photometry, so we take the actual photometric error as 15%, except for the two objects fainter than AB magnitude 24.7 in F110W, in which the internal statistical error dominates (giving errors of 0.2–0.3 mag). The grism data were processed using the NICMOSLOOK routine to produce a synthetic flat field at each spectral pixel based on the wavelength of the dispersed light from the associated object as identified from the direct image and subsequent extraction of the spectra with windows optimized for the signal-to-noise ratio. A synthetic flat field was generated for each extracted spectrum, interpolating between narrowband flats to derive the sensitivity appropriate to the wavelength corresponding to each pixel for the object’s position. The filters used to generate these flats are concentrated near 1.1, 1.6, and  $1.9 \mu\text{m}$ , and the filter curves suggest that linear interpolation between flats may generate fractional errors of 10% in the flat-field structure at the least constrained wavelengths near  $1.3 \mu\text{m}$ . However, the wavelength region of redshifted  $\text{H}\beta$  and  $[\text{O III}] \lambda 5007$  (from  $1.65$ – $1.70 \mu\text{m}$ ) is well constrained by this process, so that flat-field errors in this spectral range are minimal. For emission-line objects too faint to have their spectra automatically extracted, we sought emission lines by examining the grism images at the  $(x, y)$ -locations given by the object’s coordinates in direct images and the predicted wavelength of  $[\text{O III}] \lambda 5007$ , based on the dispersion relation for the G141 disperser from the NICMOS Data Handbook (Version 3.0). The tilt angle between the dispersion axis and detector rows can change with time and was derived from the data themselves using spectra of bright stars. In two cases, we have formal detections of  $[\text{O III}]$  line emission from these faint  $\text{Ly}\alpha$  emitters that are significant above the  $2\sigma$  level.

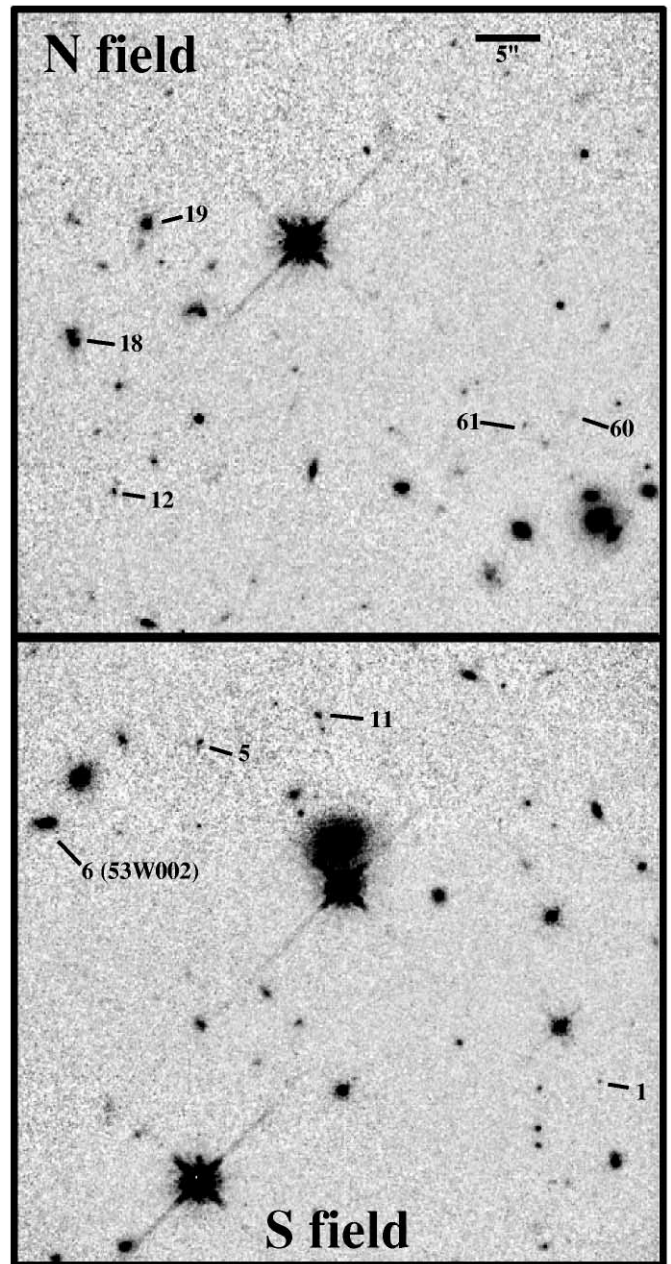


Fig. 2.—Drizzled NIC3 images in F160W ( $1.6 \mu\text{m}$ ) for the two overlapping fields observed displayed with a linear intensity mapping. Each field subtends  $46''.5 \times 46''.5$ . The instrumental  $(x, y)$ -coordinates are oriented close to cardinal directions, as shown in Fig. 1. For the northern field, the instrumental  $+x$ -axis, which runs vertically as displayed here, points  $3^\circ 9'$  west of north, while for the southern field it points  $0^\circ 6'$  east of north. The three dithered subpointings for each field were offset 8.3 NIC3 pixels along the  $x$ -axis (approximately north-south) from one another. High-redshift objects from Fig. 1 are marked. All three AGNs exhibit resolved structure, dominated by redshifted  $[\text{O III}]$  emission. For objects 6 and 19, these coincide with ionization/reflection cones seen in the UV emission lines, while for object 18 the structure is brighter and more complex. For orientation of the two fields on the sky, the same objects appear at the bottom left corner of the northern field and the top right corner of the southern field.

## 2.2. Ground-based $2 \mu\text{m}$ Imaging

We used the 3 m NASA Infrared Telescope Facility in 1996 July and 1997 April to observe the 53W002 region in  $K$  and in redshifted  $\text{H}\alpha$  with the  $256 \times 256$  pixel NSFCAM array configured for  $0''.30$  pixels. The  $\text{H}\alpha$  data used a circu-

TABLE 2  
INFRARED EMISSION LINES IN AGNs

Name	$K$	$F(\text{H}\alpha + [\text{N II}])^a$	EW	$F([\text{O III}])$	EW	$F(\text{Ly}\alpha)$
W02.....	18.55	$1.7 \times 10^{-15}$	345	$2.5 \times 10^{-15}$	701	$2.8 \times 10^{-16}$
18.....	19.39	$6.3 \times 10^{-16}$	221	$2.2 \times 10^{-15}$	600	$4.7 \times 10^{-16}$
19.....	18.55	$4.0 \times 10^{-16}$	81	$8.9 \times 10^{-16}$	89	$8.0 \times 10^{-16}$
Cyg A...	...	$1.7 \times 10^{-13}$	693	$1.6 \times 10^{-13}$	678	...

<sup>a</sup> Line fluxes are in  $\text{ergs cm}^{-2} \text{s}^{-1}$ , and equivalent widths are in angstroms in the emitted frame.

lar variable filter (CVF) tuned to  $2.22 \mu\text{m}$ . We measured the filter bandwidth to be  $\text{FWHM} = 0.040 \mu\text{m}$  ( $\Delta z = 0.05$  for redshifted  $\text{H}\alpha$ ) from a spectral scan of NGC 7027 in  $\text{Br}\gamma$  and the adjacent  $\text{H}_2 \text{S}(1)$  line (at  $2.166$  and  $2.247 \mu\text{m}$ , respectively). Individual  $K$  exposures were 10 s, coadded in groups of six before saving to disk, while exposures through the CVF were 60 s long. From two observing runs, we obtained total integrations of 3.9 and 10.9 hr in the  $K$  filter and CVF, respectively. The effective integration time per pixel varies substantially across the field because of both short- and long-timescale dithering. Flux calibration used UKIRT faint standard stars (Hawarden et al. 2001).

To account for changes in the near-IR atmospheric emission spectrum on timescales of hours, we constructed sky frames from sliding clipped means of data subsets. The seeing varied widely during the single night of 1996 observations, so we rejected images with poor image quality as assessed from bright field stars. The 1997 data suffered from a slowly time-variable PSF because of changes in the mirror figure with hour angle, so they were stacked into approximately 1 hr blocks coinciding with changes in filter or large-scale dithering. The region of 53W002 itself was covered mostly in the 1996 data, while the area including the  $\text{Ly}\alpha$

emitters to its west was included in both data sets, so we analyze these objects from the overall sum. For pure continuum objects, the count rate ratio between narrowband and  $K$ -band images is consistent within 2% over the range of colors encountered in this field, so we can use this ratio as a straightforward indicator of line emission within the CVF passband. The three AGNs (53W002 itself and objects 18 and 19 of P96) are strong  $\text{H}\alpha + [\text{N II}]$  sources, with spatially integrated line fluxes from the NICMOS and IRTF observations as listed in Table 2. The table includes equivalent widths in angstroms in the emitted frame; the nearby narrow-line radio galaxy Cygnus A is included for comparison from data in Owen, O’Dea, & Keel (1990) and Osterbrock & Miller (1975). The  $\text{H}\alpha$  emission from 53W002 is spatially resolved, elongated east-west (Fig. 3), roughly matching the structure seen for  $\text{Ly}\alpha$  in WFPC2 imaging and for  $[\text{O III}]$  in the NICMOS spectrum.

We detected none of the  $z = 2.4$  star-forming objects in  $\text{H}\alpha + [\text{N II}]$  line emission, giving lower limits to the  $\text{Ly}\alpha/\text{H}\alpha$  ratio. The detection thresholds vary somewhat with position because of different effective integration times after mosaicking the various sets of pointings. Typical limits on  $\text{H}\alpha + [\text{N II}]$  flux are around  $1.1 \times 10^{-16} \text{ergs cm}^{-2} \text{s}^{-1}$ .

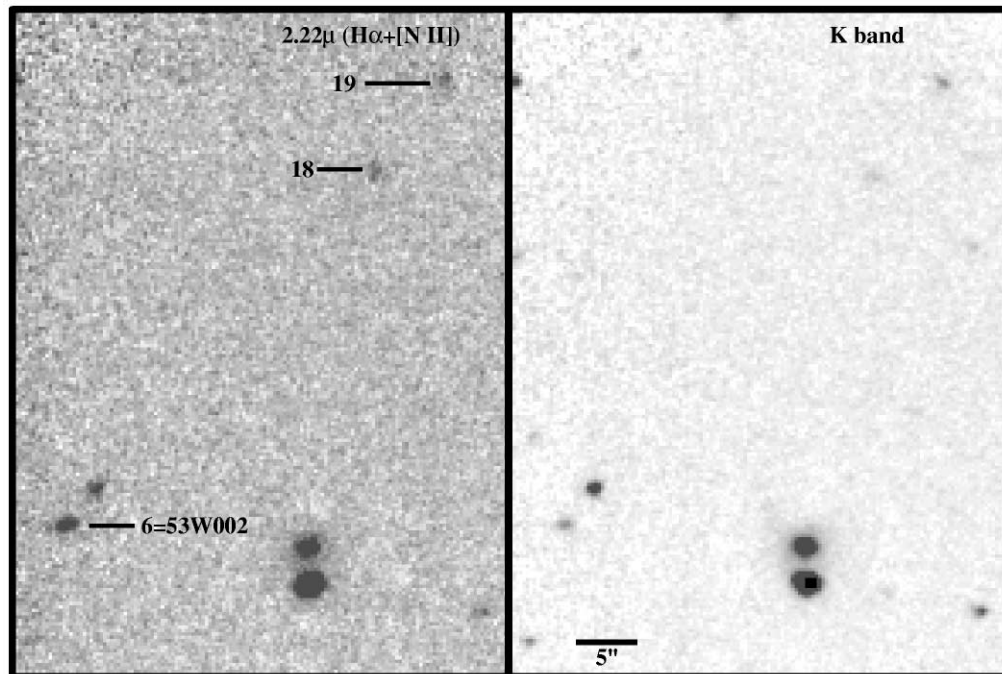


FIG. 3.—Matching sections of the stacked IRTF images in the CVF passband including  $\text{H}\alpha + [\text{N II}]$  (left) and broadband  $K$  (right). North is at the top and east to the left across a  $43'' \times 58''$  area. The images are approximately scaled in intensity so that a pure continuum object has the same brightness in both. The strong emission in object 6 stands out and is seen at a less impressive level in 18 and 19.

TABLE 3  
BROADBAND PHOTOMETRY OF STAR-FORMING OBJECTS

Object	$z$	$F_B^a$	$F_V$	$F_I$	$F_{110}$	$F_{160}$	$F_{175}$	$F_K$
01.....	3.1: <sup>b</sup>	0.74	0.62	0.39	-0.05	-0.49	...	0.49
05.....	2.048	0.90	0.75	0.48	0.29	0.14	...	...
11.....	2.451	0.78	0.62	0.40	0.15	0.21	...	...
12.....	2.053	0.98	0.75	0.61	0.37	0.05	0.03	...
60.....	2.30:	0.64	0.38	0.11	0.09	-0.42	0.18	0.50
61.....	...	0.28	0.08	0.11	-0.45	-0.36	...	...
AGN:								
06.....	2.390	1.22	1.25	1.19	1.10	1.23	...	1.16
18.....	2.393	1.29	1.10	0.93	0.85	1.12	0.94	0.83
19.....	2.397	1.31	1.13	1.00	1.03	1.10	1.02	1.06

<sup>a</sup> Fluxes are in  $\log(F_\lambda/10^{-19} \text{ ergs cm}^{-2} \text{ s}^{-1} \text{ \AA}^{-1})$ .

<sup>b</sup> Redshift uncertain from one possible feature, assumed Ly $\alpha$ .

### 3. SPECTRAL ENERGY DISTRIBUTIONS

We combine the integrated fluxes from the NICMOS data with new measurements from the earlier WFPC2 observations (P96; P98) to define the broadband spectral shape of the star-forming objects over the 1100–6500 Å emitted range. The WFPC2 fluxes have been improved through “on-the-fly” reprocessing with improved flat fields and bad pixel maps, as compared with the earlier analysis. The relevant fluxes are given in Table 3, listed as the equivalent flux density at band center for a flat spectrum. For brevity, we denote measures through WFPC2 filters by their nearest standard photometric equivalents:  $B$  (F450W),  $V$  (F606W), and  $I$  (F814W).

As shown in Figure 4, the objects are quite blue across this entire spectral range, immediately suggesting that the stellar populations are both young and metal-poor (since

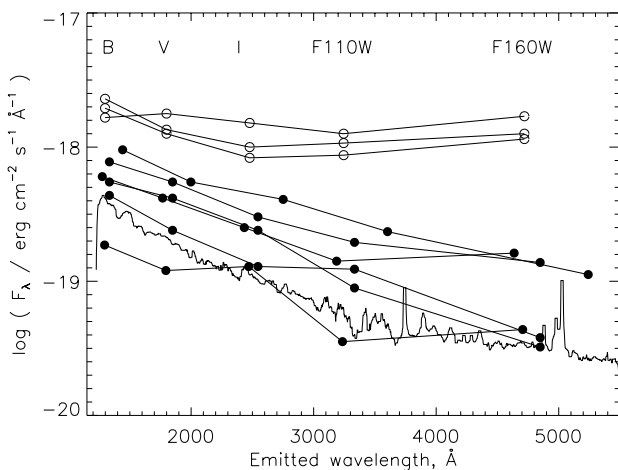


FIG. 4.—Comparison of the SEDs as used in fitting the slope parameter  $\beta$ . The three AGNs, at the top in flux, are shown as connected open circles, while the fainter star-forming objects are shown with connected filled circles. Since some of these objects are at redshifts different from the  $z = 2.39$  of the 53W002 grouping, the fixed passbands introduce a visible dispersion in the effective emitted wavelengths of their flux data. Comparison of various photometric recipes suggests typical errors of 0.15 mag for the three shorter wavelength WFPC2 bands and 0.30 mag for the two NICMOS bands, largely driven by uncertainties in the curve of growth for slightly resolved objects; individual error bars are not plotted to reduce clutter. For comparison, we overlay a smoothed composite  $IUE$ /optical integrated spectrum of the blue compact dwarf galaxy UGC 9560 as presented by McQuade, Calzetti, & Kinney (1995).

such a steep slope leaves little scope for dust reddening). The three spectroscopically identified AGNs distinguish themselves from the putative star-forming objects not only in flux but in having substantially flatter spectra in  $F_\lambda$ . To investigate the age and allowed metallicities of the star-forming objects, we follow the precepts of Calzetti, Kinney, & Storchi-Bergmann (1994) in using the UV slope parameter  $\beta$  (where  $F_\lambda \propto \lambda^\beta$  as fitted across the 1200–2600 Å range). This was derived by least-squares fitting in the log domain (Table 4). Many of the derived errors cluster closely because much of the overall photometric error comes from either possible scale errors or aperture effects and is thus not a very strong function of flux.

Calzetti et al. find that the intrinsic spectral slope of model populations in the extreme cases of an instantaneous burst (less than  $2 \times 10^7$  yr old, to keep substantial ionizing flux) and continuous star formation at a constant rate differ by no more than 13% in slope about the  $\beta = -2$  reference point over the 1200–2600 Å span of good  $IUE$  spectra, so that the observed slope of a star-forming system can be used to estimate the effective reddening. Using large-aperture integrated spectra, so that we deal with scattering and mixing of multiple star-forming regions in a way appropriate for comparison with the integrated properties we measure for the high-redshift objects, they show that nearby systems follow a correlation between slope of the UV spectral energy distribution (SED) and emission-line abundances, for a plausible reddening-metallicity correlation. Our slope measurements, being based on a few broadband data points, are

TABLE 4  
FITTED CONTINUUM  
SLOPES  $\beta$

Object	$\beta$
01.....	$-2.26 \pm 0.14$
05.....	$-1.41 \pm 0.09$
11.....	$-1.15 \pm 0.11$
12.....	$-1.62 \pm 0.11$
60.....	$-1.77 \pm 0.17$
61.....	$-1.27 \pm 0.28$
AGN:	
06.....	$-0.08 \pm 0.14$
18.....	$-0.44 \pm 0.22$
19.....	$-0.44 \pm 0.23$

necessarily less sophisticated than the targeted spectral windows used by Calzetti et al. As noted by Bell et al. (2002), the difference in  $\beta$ , as derived from fitting in the purest continuum windows and from images in these broad passbands, gives a typical error of  $\pm 0.2$ , comparable to our purely observational statistical errors. We derive values  $\beta = -1.1$  to  $-2.3$  from fits across the entire observed range from  $0.45$  to  $1.6 \mu\text{m}$  for the star-forming objects in the 53W002 grouping (Table 4). Slopes over subsets of this spectral range are consistent but give larger internal errors (and scatter), ranging from  $-1.4$  to  $-2.4$  between  $0.55$  and  $1.1 \mu\text{m}$ . Only a few nearby star-forming objects have continua this blue; Calzetti et al. (1994) list only NGC 1705, UGC 9560, and Tol 1924-416 having  $\beta < -1.8$ , while Meurer, Heckman, & Calzetti (1999) add seven more (NGC 4861 and Mrk 153 at  $\beta < -2.0$  plus Mrk 66, NGC 3991, NGC 3738, UGCA 410, and Mrk 357 with  $-1.8 > \beta > -2.0$ ). All these are classified as blue compact galaxies rather than within the ordinary Hubble types. Three of the six objects in the 53W002 field fall in this regime.

Although the correlation between spectroscopically derived  $[\text{O}/\text{H}]$  and  $\beta$  has substantial scatter [ $\pm 0.2$  in  $\log(\text{O}/\text{H})$  at  $12 + \log(\text{O}/\text{H}) = 8.3$ , with the scatter greatest at low metallicity], the only nearby systems as blue as objects 1, 12, and 60 in this sample have  $12 + \log(\text{O}/\text{H}) < 8.5$ , which implies less than half solar [ $12 + \log(\text{O}/\text{H}) = 8.82$ ]. The extreme low-abundance dwarf I Zw 18 falls in this range, with  $\beta = -2.43$  from Meurer et al. (1999) and  $12 + \log(\text{O}/\text{H}) = 7.18$  from Izotov & Thuan (1999). The color-abundance relation clearly flattens at such low values, but even so, the metal abundances implied by the blue colors are low enough to suggest that we are seeing genuinely lower abundances at  $z = 2.4$  than are found in the most similar systems today. This is illustrated in Figure 5 by both the observed and dereddened UV luminosities of the 53W002 star-forming objects, most of which fall outside the range of luminosity and  $\beta$  populated by local objects.

Low metallicities for these systems are especially interesting in view of the high UV luminosities and derived star formation rate. In a simple picture of starbursts in an interstellar medium (ISM), the metallicity of the gas may reflect a combination of preburst conditions and metals expelled from the first supernovae of the starburst population itself. One might then expect a given starburst to have greater metallicity in the present universe, after many gigayears of previous star formation has enriched the ISM, compared to the early universe, in which the burst we observe may mark the first significant episode of star formation. Enrichment to about the SMC level should be quite rapid, on the order of  $10^7$  yr, unless the enriched material is quickly mixed with large amounts of pristine gas (Izotov & Thuan 1999; Kobulnicky 1998). The general luminosity-metallicity relation can be examined for differences in locus between local and high-redshift, star-forming objects. To do this, we compare metallicities with UV luminosities at emitted wavelengths  $1100\text{--}1300 \text{ \AA}$ , for which *IUE* and *HST* data are available on nearby objects (from Calzetti et al. 1994 and Meurer et al. 1999, augmented by  $[\text{O}/\text{H}]$  measures for I Zw 18 and NGC 4861 from Izotov & Thuan 1999). We consider sets of cosmological parameters with  $H_0 = 60\text{--}80 \text{ km s}^{-1} \text{ Mpc}^{-1}$  and both  $\Omega_M = 1$  and  $\Omega_M = 0.3$ ,  $\Omega_\Lambda = 0.7$ . These combinations, at  $z = 2.4$ , give ranges of linear scale from  $4.9$  to  $9.5 \text{ kpc arcsec}^{-1}$  and luminosity distances of  $D_L = 11.6\text{--}22.6 \text{ Gpc}$  at look-back times of  $6.8\text{--}12.5 \text{ Gyr}$

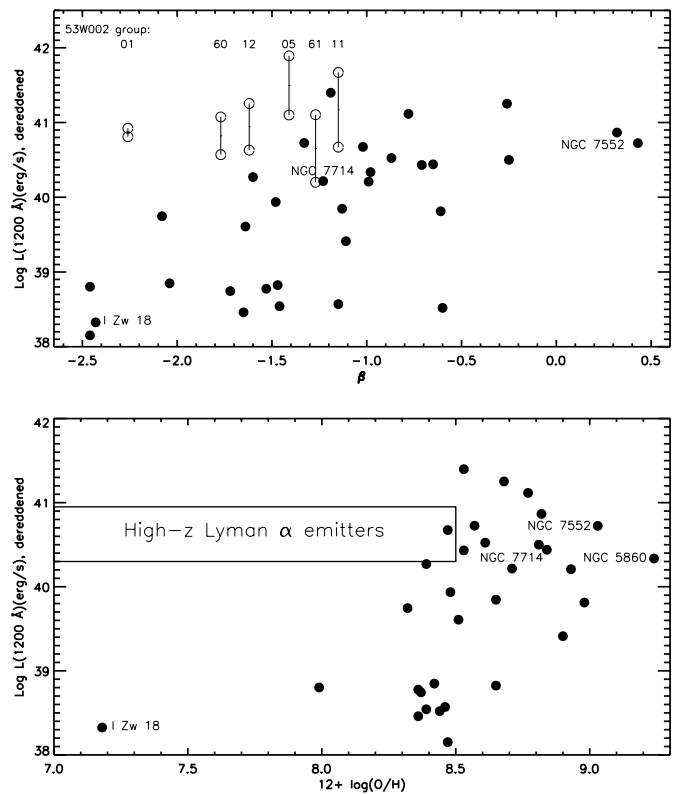


FIG. 5.—Relations between UV luminosity  $L(1200)$  and spectral index  $\beta$  (top) and spectroscopically measured  $\text{O}/\text{H}$  (bottom). Filled circles show local objects, with well-known and extreme examples named, while open circles are star-forming objects in the 53W002 field. The vertical pairs of open circles in the top panel indicate values as observed and the amount of reddening correction from the Meurer et al. (1999) prescription. In both diagrams, the high-redshift objects extend into ranges of parameter space including a low-metallicity/high-luminosity combination not found in the local comparison sample. Since only limits to the metallicity are available from  $\beta$ , the whole sample of high-redshift objects is represented by an open-ended box in the abundance panel.

and cosmic ages of  $1.2\text{--}3.1 \text{ Gyr}$ . Thus for these high-redshift objects the luminosities we derive will vary by a factor 4, depending just on the adopted cosmology; in Table 5, we quote the geometric mean of these extremes. Smaller  $H_0$  and larger  $\Lambda$  increase the derived luminosity. The star-forming objects in the NICMOS fields all fall within the range  $1.5\text{--}9 \times 10^{40} \text{ ergs s}^{-1} \text{ \AA}^{-1}$  in this (emitted) passband, quite luminous indeed. The only object well within this luminosity range in the *IUE* sample used to derive the local relationships is Mrk 357 ( $z = 0.05$ ,  $L_{1200} = 5.7 \times 10^{40}$ ). A metallicity-luminosity relation appears in the data for

TABLE 5  
DERIVED UV AND OPTICAL  
CONTINUUM LUMINOSITIES

Object	$L(1200)^a$	$L(5000)$
1 <sup>b</sup> .....	$3.1 \times 10^{40}$	$3.5 \times 10^{39}$
5 .....	$8.9 \times 10^{40}$	$9.7 \times 10^{39}$
11 .....	$4.7 \times 10^{40}$	$1.8 \times 10^{40}$
12 .....	$4.3 \times 10^{40}$	$8.0 \times 10^{39}$
60 .....	$3.7 \times 10^{40}$	$4.1 \times 10^{39}$

<sup>a</sup> Luminosities are in  $\text{ergs s}^{-1} \text{ \AA}^{-1}$ .

<sup>b</sup> Assumed at  $z \approx 2.4$ .

$12 + \log(\text{O}/\text{H}) < 8.6$ , above which extinction corrections become large enough that the star-forming regions are dimmer when using uncorrected data. The important point is that the objects at  $z > 2$  occupy a region in this plane that contains no nearby examples (Fig. 5).

The most luminous nearby object with  $12 + \log(\text{O}/\text{H}) < 8.5$  is Mrk 66 at 8.39 and  $L(\text{UV}) = 4 \times 10^{39} \text{ ergs s}^{-1} \text{ \AA}^{-1}$ , which is 4–20 times less luminous than the high-redshift objects (so there is no overlap for any of the cosmologies we consider). The gap grows for lower  $[\text{O}/\text{H}]$  values. Correction for internal absorption, which we do following Meurer et al. (1999) in taking  $dA_{1600}/d\beta = 1.99$ , does not change this situation, although it does increase some luminosities by an order of magnitude (Fig. 5).

These stellar populations cannot be extremely young bursts (a few  $10^6$  yr) or the optical line equivalent widths would be very high against the combined nebular and stellar continuum (as in Mrk 490, observed by De Robertis & Osterbrock 1986); the equivalent width of  $\text{H}\beta$  saturates against the recombination continuum at 1350 Å. The continuity between WFPC2 and NICMOS fluxes and the comparably good fit of the power law across the whole observed range shows that the emerging light is dominated by young populations. We see no clear evidence of any upturn at longer wavelengths that would come from a significant redden and older population (§ 6). Thus the populations do not furnish us the leverage needed for a detailed fit to models of various ages or mixed populations involving multiple star-forming episodes.

#### 4. EMISSION LINES IN THE STAR-FORMING OBJECTS

Examination of individual pixels around the predicted location of the  $[\text{O III}]$  lines shows detections of  $\lambda 5007$  ( $2\text{--}4 \sigma$  at independently specified wavelengths) in two of the star-forming objects that are brightest at  $1.6 \mu\text{m}$ , object 11 at  $z = 2.451$  and object 12 at  $z = 2.05$ . This procedure gave higher signal-to-noise ratio than the standard NICMOS-LOOK spectral extraction for detecting faint and narrow emission features, whose results showed no significant line emission in either  $\text{H}\beta$  or  $[\text{O III}]$ . Crosscuts through the grism images, showing emission at the expected wavelengths of  $[\text{O III}]$ , are shown in Figure 6. Both these objects show double morphologies in WFPC2 F450W images, which might either represent merging or multiple star-forming regions in a single galactic potential. In combination with the  $\text{Ly}\alpha$  fluxes and SED slopes, even our upper limits for lines redshifted into the near-IR set interesting constraints

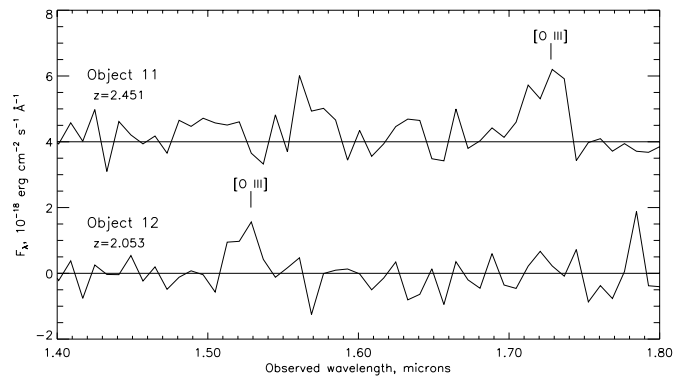


FIG. 6.—Slices through the NICMOS grism spectra at the expected locations of  $[\text{O III}] \lambda 5007$ , showing detections in the two star-forming objects 11 and 12 at  $z = 2.45$  and  $2.05$ . These are  $0''.6$  width extractions, with scattered light from nearby objects subtracted using a 25 pixel boxcar filter. The data for object 11 have been offset vertically, with the zero flux line plotted. The expected location of the stronger  $[\text{O III}]$  line  $\lambda 5007$  is marked in each case. Emission is detected from these two objects at about the  $3 \sigma$  level, although at low levels the statistics are not quite Gaussian. The implied line fluxes are  $1\text{--}2 \times 10^{-16} \text{ ergs cm}^{-2} \text{ s}^{-1}$  for equivalent widths  $100\text{--}130 \text{ \AA}$  in the emitted frame using the broadband images for continuum flux.

on the effective ages and metallicities of these objects. The measurements and upper limits are given in Table 6. For comparison, upper limits to  $\text{H}\alpha$  emission for these objects (§ 2.2) are typically  $7 \times 10^{-17} \text{ ergs cm}^{-2} \text{ s}^{-1}$ . This already indicates a minimal role for dust, since the  $\text{Ly}\alpha/\text{H}\alpha$  ratio is required to be larger than encountered in nearby star-forming systems (e.g., Giavalisco, Korotkar, & Calzetti 1996); lower limits for the ratio range from 0.3–3 for various objects. The  $\text{H}\alpha$  limits imply upper limits on  $\text{H}\beta$  slightly more stringent than do the NICMOS spectra themselves, typically  $2 \times 10^{-17} \text{ ergs cm}^{-2} \text{ s}^{-1}$ , for those objects at  $z = 2.39 \pm 0.013$  (including, as it happens, neither of the objects with possible  $[\text{O III}]$  detections, since their redshifts fall outside the range for bona fide group members for which the narrow CVF  $\text{H}\alpha$  filter was tuned).

The continuum slopes make it clear that these objects must be in the low-metallicity regime, so they are likely to fall on the lower branch of the relation between  $[\text{O III}]/\text{H}\beta$  and  $[\text{O}/\text{H}]$  often used to estimate metallicities for faint objects by the “bright line” method (introduced by Pagel et al. 1979). The line limits (and possible  $[\text{O III}]$  detections) can put combined constraints on the duration of star formation and metallicity. Significant star formation is still in progress as we see these objects, since there is enough ionizing radiation to power the  $\text{Ly}\alpha$  emission, although radiative transfer

TABLE 6  
EMISSION-LINE PROPERTIES FOR STAR-FORMING OBJECTS

Object	$\text{Ly}\alpha^a$	$[\text{O III}] \lambda 5007$	$\text{H}\beta$	$\text{EW}(5007)^b$	$\text{EW}(\text{H}\beta)$
1.....	$2.6 \times 10^{-17}$	$<4 \times 10^{-17}$	$<4 \times 10^{-17}$	$<360$	$<360$
5.....	$1.7 \times 10^{-16}$	$<4 \times 10^{-17}$	$<4 \times 10^{-17}$	$<95$	$<95$
11 <sup>c</sup> .....	$3.4 \times 10^{-17}$	$1.9 \times 10^{-16}$	$<8 \times 10^{-17}$	340	$<140$
12.....	$3.4 \times 10^{-16}$	$1.3 \times 10^{-16}$	$<4 \times 10^{-17}$	380	$<120$
60.....	$3.1 \times 10^{-17}$	$<4 \times 10^{-17}$	$<4 \times 10^{-17}$	$<320$	$<320$

<sup>a</sup> Line fluxes are in  $\text{ergs cm}^{-2} \text{ s}^{-1} \text{ \AA}^{-1}$ .

<sup>b</sup> Equivalent widths are in the emitted frame. The continuum was derived from F160W images, since it is too weak to be measured in the NICMOS spectra.

<sup>c</sup> Superposed on the spectrum of a brighter object.

effects mean that we cannot use its intensity by itself as a reliable estimator of the rate of star formation. The equivalent width of  $H\beta$  was considered as an age indicator by Copetti, Pastoriza, & Dottori (1986). We use the more recent models presented by Stasinska & Leitherer (1996). Effective burst ages in the range  $(3-8) \times 10^6$  yr satisfy the equivalent width limits for the emitted-optical lines while still having strong  $Ly\alpha$ . The  $H\beta$  limits rule out very young, high ionization starbursts; there must be enough cooler stars to contribute diluting light to the continuum around  $H\beta$ . Photospheric absorption in the stellar populations will be small compared to these limits; the largest equivalent widths seen in main-sequence stars are  $13.5 \text{ \AA}$ , from the data presented by Jacoby, Hunter, & Christian (1984), while the largest values for model populations with a Salpeter-like initial mass function are only  $4 \text{ \AA}$ .

Stasinska & Leitherer note that there is a small spread in model parameters needed to reproduce the observed properties of low-metallicity starbursts, so that the  $[O \text{ III}]$  equivalent width is also useful as an age indicator. Using their models for metallicity 0.25 and 0.1 solar, the  $H\beta$  limits imply equivalent burst ages greater than  $2.5 \times 10^6$  yr for the high limits and  $4 \times 10^6$  yr for the lowest limit (object 5). For the two nominal detections of  $[O \text{ III}]$ , its equivalent width gives broadly concordant ages,  $(2-5) \times 10^6$  yr for the relevant metallicity range. If these detections are valid, they put lower limits on the gas metallicity, since the implied  $[O \text{ III}]/H\beta$  is greater than three for these two objects. However, again following the models published by Stasinska & Leitherer (1996), these limits only imply that the abundances are less than solar, since the predicted line ratios (in the age range matching the equivalent widths) are high for all the abundances they considered. This is much less stringent than limits from the continuum slope, although refinement from ground-based data is now possible using IR spectrometers on 8–10 m telescopes. We note that the two objects with  $[O \text{ III}]$  detections are the reddest and presumably most metal-rich of the NICMOS sample, which fits with the picture that these are all on the low-metallicity branch of the relation between  $O/H$  and  $[O \text{ III}]/H\beta$ , so that lower  $O/H$  in fact weakens  $[O \text{ III}]$  emission.

There is a dual paradox in the combination of high rates of star formation needed for the observed ultraviolet luminosity, low metallicity, and number of objects seen in the small volume of the 53W002 grouping. If these are continually forming stars over a long time, we should see low abundances in a closed-box system for only a very short time and might expect to see a much larger number of older systems with redder colors and higher metallicities, which the source counts in this field do not allow. If indeed they have all begun star formation only  $\approx 10^7$  yr before our view, it seems unusual good fortune that they have done so nearly simultaneously so that we see so many at once. We might thus consider pictures in which such systems might be observable with these properties for longer times and ask what kinds of present-day galaxies they might become.

Episodic star formation makes some of these issues more tractable, although still suggesting that there are more similar objects in a dim state by a factor related to the duty cycle of active star formation. Such episodes might be triggered by the equivalent of mergers (although now for systems that might or might not already be considered distinct galaxies and might not yet have undergone important levels of star formation). This notion has some support from the fact that

half of star-forming objects in our sample have double structure on 2–5 kpc scales and the well-documented relation between tidal interactions and star formation in the present universe. This mechanism lengthens the time span over which the objects are (sometimes) bright but does not address the low-metallicity issue.

There is substantial evidence that global winds (superwinds) were important during the early phases of galaxy evolution. Powerful winds are suggested for high-redshift galaxies by strong and slightly redshifted  $Ly\alpha$  emission (e.g., Pettini et al. 2001) by the amount of early enrichment needed to account for abundances in the intracluster and intergalactic media (Tripp, Savage, & Jenkins 2000) and by a connection between strong  $Ly\alpha$  and global winds for starburst galaxies (Keel 2002). At low redshifts, the fossil record of dwarf galaxies and ongoing winds in starbursting dwarfs suggest that many low-mass galaxies have been swept clean by winds rather than being able to self-enrich with processed material for long times (Marlowe et al. 1995).

Winds from the star-forming objects we see at  $z > 2$  would help explain both the strong  $Ly\alpha$  emission and low abundances, since processed gas would be removed as fast as it is produced. If this only happens once, these objects are not the progenitors of any obvious present-day galaxy population, but multiple cycles of gas inflow and outflow could yield an interesting stellar mass and slow buildup of metals. Such cycles could ameliorate the fading problem, giving a final stellar mass that corresponds at least to current dwarf systems. Our direct limits on the star-forming histories of these objects are not very strong (§ 6), although we can say that they allow a mass in stars (for a Salpeter-like initial mass function) that is an order of magnitude greater than the mass of stars with age less than  $10^7$  yr, so that in principle many similar episodes could have occurred.

## 5. STRUCTURE AROUND AGNs IN THE EMISSION LINES AND CONTINUUM

Observations in the emitted UV have shown extended structure around all three bright AGNs in this field, as seen in  $Ly\alpha$  (Windhorst et al. 1998; Keel et al. 1999), an interestingly high fraction even if one based on small numbers. The brightest parts of the extended emission are elongated and in two cases roughly triangular with the nucleus at the apex. In line with observations of many other AGNs, such structures may fairly be interpreted as ionization or scattering cones, an idea we explore using these data. Further information on these features might distinguish the roles of scattering and in situ line emission and to tell whether this material is part of outflows driven by the AGNs or might represent ambient (enriched) material. The near-IR data show these structures as traced by  $H\alpha$  and  $[O \text{ III}] \lambda\lambda 4959, 5007$ , adding not only new ions but new combinations of spatial and spectral resolution. The line intensities and equivalent widths are given in Table 2, along with  $Ly\alpha$  fluxes from Pascarella et al. (2002) for comparison. The NICMOS spectra are shown in Figure 7. At this redshift,  $[O \text{ II}] \lambda 3727$  falls in a region of poor throughput, so it was not clearly detected in any of these AGNs.

The  $Ly\alpha/H\alpha$  ratios for the three AGNs range from 0.2 (53W002) to 2.0 (object 19). Values near two are usual for nearby narrow-line radio galaxies over a wide range of ionization (Keel & Windhorst 1991).  $H\beta$  is not clearly detected in any of these objects. It would appear 6 pixels blueward of

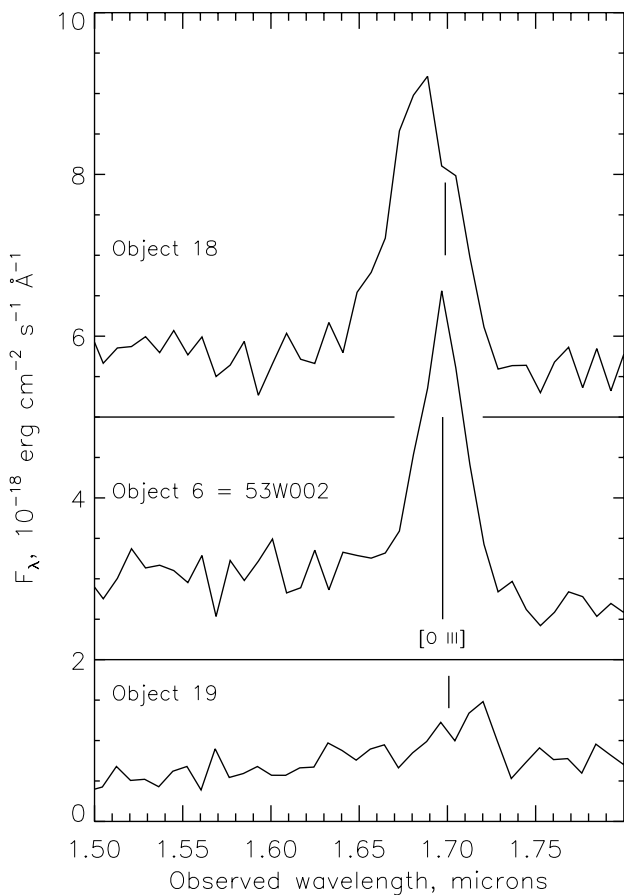


FIG. 7.—NICMOS grism spectra of the three AGNs in the 53W002 grouping, covering the regions around redshifted  $H\beta + [O\text{ III}]$ . Much of the apparent line width in 53W002 itself and object 18 is due to spatially resolved emission, as seen in  $Ly\alpha$  and  $H\alpha$ . The spectra of objects 6 and 18 have been offset vertically by  $2$  and  $5 \times 10^{-18}$  ergs  $\text{cm}^{-2} \text{s}^{-1} \text{\AA}^{-1}$ , respectively, with their zero-flux lines plotted. The location of  $[O\text{ III}] \lambda 5007$  at the redshift of  $Ly\alpha$  is shown by vertical lines. The  $[O\text{ III}]$  peaks, especially in object 18, are shifted from the expected wavelength based on the redshift of  $Ly\alpha$  (vertical lines) by spatially resolved structure.

the  $\lambda 5007$  peak, but the two objects with strongest  $[O\text{ III}]$  show spatially extended emission such that the monochromatic  $[O\text{ III}]$  emission overlaps the location of  $H\beta$ . A multi-component fit to the profile in 53W002 gives a formal value  $H\beta/[O\text{ III}] = 0.06$ , best taken as an upper limit. Ratios this large are common in narrow-line AGNs, such as Cyg A (Costero & Osterbrock 1977).

We note that the emitted-ultraviolet spectra (Pascarelle et al. 2002) of these three AGNs, like essentially all others where the spectrum is not compromised by broad absorption features, show solar or supersolar metallicities for the broad-line regions. Hamann et al. (2002) find that the nitrogen abundance is most robustly measured from strong UV lines, especially  $\lambda 1240$ , and that formation of massive stars must have been active for  $\approx 10^8$  yr to yield such enrichment. This is in stark contrast to the low abundances derived from colors and line ratio limits in the star-forming narrow  $Ly\alpha$  sources.

The colors and emission-line structures of the extended emission around the AGNs have suggested a mix of mechanisms for their radiation. The strong and very extended  $Ly\alpha$  cloud around object 18 (Pascarelle et al. 1996; Keel et al. 1999) requires in situ photoionization, probably by an

anisotropic continuum source. However, the NICMOS spectrum shows that the continuum at  $1.5\text{--}1.6 \mu\text{m}$  is spatially resolved, spanning a  $1''.4$  range, suggesting that scattering is also important (whether or not we have a direct view of the nucleus). The nature of the putative scattering medium is important for understanding the history of star formation in the AGN hosts. If dust is responsible, we have very different conditions in the AGN host galaxies, which are metal-rich enough to be producing substantial dust for transport over tens of kiloparsecs, while their non-AGN neighbors are so metal-poor that we see only mild evidence of internal extinction in the ultraviolet. This correlation between derived metallicity and presence of an AGN suggests that the low-luminosity star-forming objects have not yet hosted a powerful AGN. The extent of transport of the dust and enriched gas might be important in some cases if it can interact with the nearby star-forming systems.

### 5.1. Reflection Nebulosity in Object 18

Object 18 has complex extended structure in  $Ly\alpha$  emission (Pascarelle et al. 1996; Keel et al. 1999). The roles of ionization and reflection are not well separated by earlier imaging data, and the grism spectrum provides new evidence that reflection (presumably from dust many kiloparsecs from the nucleus) plays a significant role. A crosscut through the grism data perpendicular to the dispersion (which is almost north-south) shows that its image is resolved and distinctly double. Such resolution might be due to a genuinely complex starlight distribution or to scattering of radiation from the AGN. A contribution from scattering would be especially interesting, implying that grains are abundant and widely distributed (perhaps by global AGN-driven winds). All three AGNs in the field we observed show extended emission-line clouds at lower levels, and it is at least suggestive that these are objects with higher abundances as judged from the AGN emission lines.

A combination of scattered and in situ line emission fits with the Keck optical spectroscopy from Pascarelle et al. (2002). A slit through the extended emission about  $1''$  northeast of the core of object 18 shows strong line emission, including the C iv  $\lambda 1549$  feature (a blended doublet), which is characteristic of the dense environment in active nuclei, seen in the cloud at a level  $C\text{ iv}/Ly\alpha = 0.17$ . The ratio is somewhat larger in the core, at 0.30, but it is not obvious that we can derive relative contributions of scattered AGN light and in situ photoionization from these two ratios, since we do not know whether the core spectrum gives a direct view of the broad-line region.

The grism data furnish what amounts to a monochromatic image in  $[O\text{ III}]$  once the smooth continuum has been subtracted (shown in Fig. 8). Two prominent emission lumps appear, roughly coincident with the AGN core and the  $Ly\alpha$  cloud  $0''.6$  to its northeast as seen in the WFPC2 data. The core-to-cloud flux ratio is 0.6 in  $[O\text{ III}]$ , substantially higher than in the continuum. The mix of scattered-to-local radiation must be different on the two lines of sight; lacking confirmation of a direct view of the core, these values cannot yet specify this mix.

### 5.2. Extended Line Emission and the Host Galaxy of 53W002

Given the brightness of possibly scattered light in object 18, and since object 19 is nearly a point source, 53W002

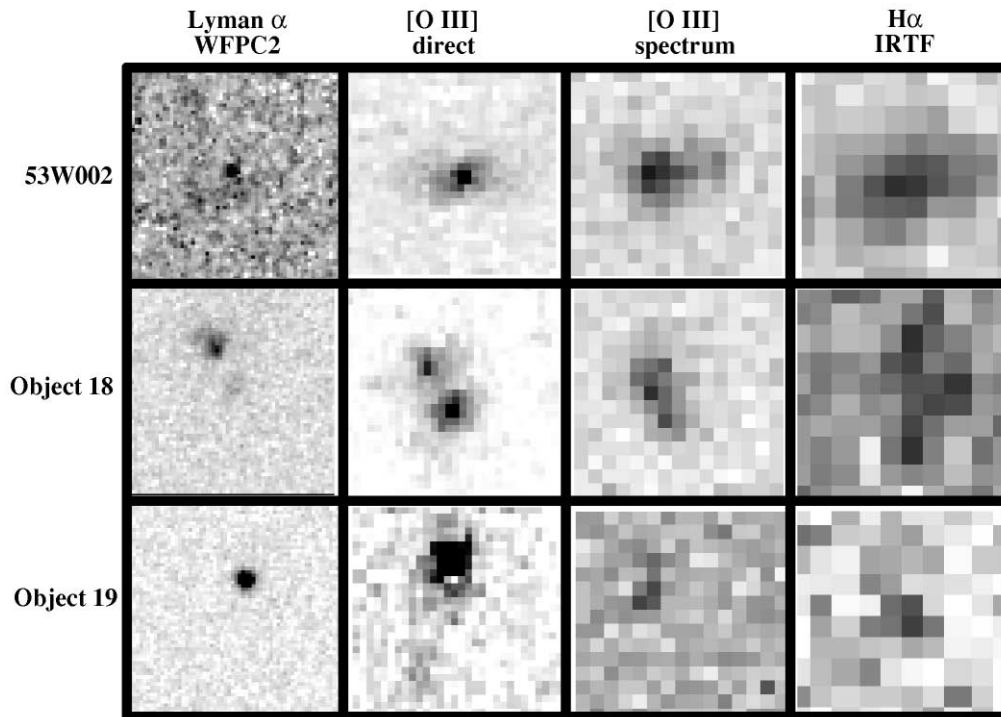


FIG. 8.—Emission-line structure of the three AGNs at  $z = 2.39$ . Each box spans  $3''$  on a side, all oriented approximately with north upward (NICMOS images are at the instrumental orientation to avoid resampling). Two [O III] images are shown. The “direct” one is from the F160W drizzle-reconstructed images, using the F110W data and a typical scale factor for approximate continuum subtraction. These images may have an improperly subtracted continuum residual at the peak. The “spectrum” image is from the slitless grism data, with the continuum subtracted by interpolation in the dispersion direction (which runs vertically here). The  $\text{Ly}\alpha$  images are from the F410M WFPC2 observations described in P96 and P98, and the  $\text{H}\alpha$  data are from the IRTF data with continuum subtraction using a scaled  $K$ -band image. Much of the most extended line emission from 53W002 and object 19 is of low enough surface brightness to be most prominent in the F160W-F110W direct image. The images of object 19 are not centered on its core to show this structure to the south-southeast. For object 18, the total line flux is dominated by the “cloud” northeast of the continuum core, and the core itself is more prominent in both [O III] renditions than in  $\text{Ly}\alpha$ .

itself is the only one of the AGNs whose host galaxy we can examine in detail. Even in this case, the imaging analysis has not been altogether straightforward in the presence of extended emission-line structure along the radio source axis, which might be accompanied by continuum reflection as well (Windhorst et al. 1998). Considerable new information is added by the Subaru spectrum of 53W002 across the  $JHK$  bands presented by Motohara et al. (2001). They detect a substantial Balmer jump in the starlight, rather than the  $4000 \text{ \AA}$  break which would be strong in populations much more than about  $10^9$  yr old. This spectroscopic analysis avoids some of the uncertainties in using the emitted-UV colors of the galaxy after removing various estimates of the contribution from the AGNs and associated extended structure (as was done in Windhorst et al. 1991, 1994, and 1998). In all cases, the age derived from the SED is less than  $5 \times 10^8$  yr.

The NIC2 F160W image and slitless spectrum can be combined to improve our separation of line emission and continuum structure in the host of 53W002. At the low dispersion of the G140 grism, the two [O III] lines are blended by the resolved emission-line structure, so that subtracting an interpolated continuum gives a good approximation to a monochromatic [O III] image (Fig. 8). The [O III] emission comes largely from two regions  $1''$  apart, situated symmetrically about the nucleus, along the same axis as the  $\text{Ly}\alpha$  extent, consistent with following the radio source axis. Line emission from the AGN core itself is rather weak, about 15% of the total flux, and the two emission regions are

unequal with almost two-thirds of the total flux coming from the western one.

We can then rotate this [O III] image, scale properly in both pixel size and intensity, and subtract it from the NIC2 broadband image to yield an improved image of the galaxy’s continuum structure alone (including the nucleus and any scattered AGN light). This passband, centered near  $4800 \text{ \AA}$  in the emitted frame, should be a better tracer of its overall stellar structure than the emitted-UV images from WFPC2. The result shows that much of the asymmetric structure in F160W, which roughly coincides with the [O III] emission, is not line contamination, but represents continuum light. The line emission accounts for about 16% of the total radiation in this passband, and its subtraction (based on the lower resolution grism data) does not change the overall morphology in this respect. This reinforces the conclusions from Windhorst et al. (1998) that there is a substantial contribution by reflection (or local, triggered star formation) along the radio axis.

## 6. OLDER HALOS AROUND STAR-FORMING SYSTEMS?

The difficulty of detecting typical galaxies at  $z > 2$  and difficulties in matching the correlation statistics of galaxies in deep fields to dynamical friction behavior have led to suggestions that many of the faint objects seen in deep fields do not represent distinct galaxies, but star-forming regions imbedded within larger dynamical entities (Colley et al.

1996, 1997). This issue is important not only for interpreting the number counts, but for our whole picture of galaxy building. We can test for the role of surface brightness and ultraviolet favoritism in our sample by seeking any redder halos around the star-forming objects and using color information to tell whether the apparent double objects might represent associations of a galactic center (presumably with a longer history of star formation) and an offset region of active star formation but less stellar mass. Redder halos are common among the rapidly star-forming systems such as blue compact galaxies (Cairós et al. 2001), in accord with studies of the stellar populations in some local star-forming galaxies (Loose & Thuan 1986; Schulte-Ladbeck et al. 1999a, 1999b, and references therein).

To make color index images of the Ly $\alpha$  emitters, we convolved the WFPC2 *B* images to match the resolution of the NICMOS data, at both F110W for better resolution and F160W to sample longward of the 4000 Å break. Because of the boxy effective PSF resulting from drizzling the NICMOS images and the different directions of diffraction structures in the two data sets, a differential PSF was constructed through deconvolution of a star seen in the NICMOS data with the same star from the WFPC2 data, after resampling them to the same pixel scale. The differential PSF had significant negative sidelobes because of the diffraction spikes and was slightly tweaked by a further Gaussian blur of 0.5 pixel (0''.05) FWHM to give neutral color gradients in the outer edges of images of bright unresolved objects.

We find no evidence of redder halos in the NICMOS data; there is a slight trend in the opposite sense to have bluer halos, although the PSF matching is sensitive enough to numerical details that we cannot claim that this tendency is real. Specific flux limits depend on how extensive the underlying redder population is taken to be. Limits to the overall amount of light from a redder population can come from the photometry. Since the SEDs are well described by the power-law forms that are empirically good fits for local star-forming systems over a wide range of metallicity, an upper limit to the amount of light from a redder population can come from considering the mean residuals at the longest wavelengths with respect to a power-law fit at shorter wavelengths. We consider excesses measured at 1.6  $\mu$ m above a power-law  $\beta$  fit to data from 0.45 to 1.1  $\mu$ m, which will be especially sensitive to populations old enough for either a strong Balmer or 4000 Å break. Of six objects, there are equal numbers with positive and negative residuals at 1.6  $\mu$ m with respect to the power law fitted to shorter wavelengths. The mean value is  $-0.01$  dex with a standard deviation of 0.20 dex. Using the standard deviation of the mean, no more than 0.08 dex (or 20%) of the flux emitted at 4800 Å comes from an older population. Any old population much brighter than this would have to be so extended and hence of such low surface brightness that it is not reflected in apertures more than 10 times the effective radius of the UV component.

The properties of the three Ly $\alpha$  emitters that show double morphologies in the WFPC2 images are also relevant to the question of whether we are really seeing the whole systems here or only star-forming pieces. Given the color and surface brightness selection biases inherent in optical detection at large redshifts, these could equally well be genuine, dynamically multiple systems or represent a nucleus and offset star-forming region. The latter case would generally give different colors for the two components, especially when

observed at redder wavelengths where any pre-existing population in the nucleus would be more prominent. The three such putative paired objects in the NICMOS fields are too close together to be clearly resolved in the NIC3 data (Fig. 9), but we can check for significant color differences between components by measuring shifts in peaks or centroids between the WFPC2 and NICMOS data when measured at a common resolution. Any such shifts are below our error levels, which are about 0.2 drizzled pixels or 0''.02 as measured from bright stellar images. This implies that the flux ratios between components in no case change by more than about 50% from *B* to 1.6  $\mu$ m. Specifically, the northern component of object 12 is about 0.3 mag brighter at 1.6  $\mu$ m than at *B* relative to its close companion 0''.27 away. Object 11 has components 0''.4 apart, just resolved in the NICMOS drizzled images. In this case as well, the intensity ratio is constant at the 30% level from *B* to F160W (about the level at which we can retrieve a value). We cannot put such a fine limit on the color of the components of object 5, since it was observed on the PC chip, which does not include enough objects to register the coordinates accurately at the subpixel level against the NICMOS data, which would be required to measure color-introduced shifts given its component separation of 0''.25. As far as we can tell from these data on close pairs of Ly $\alpha$  emitters, both components have similar star-forming properties and histories, as revealed shortward of 5000 Å in their emitted frames.

## 7. CONCLUSIONS

Comparing NICMOS and IRTF observations in the emitted-optical range to WFPC2 data in the emitted ultraviolet, we have extended our probe of the nature and evolutionary status of the 53W002 galaxy grouping at  $z = 2.4$ , considering both the three AGNs in our field and accompanying star-forming objects selected for narrow Ly $\alpha$  emission.

It is useful to compare these low-luminosity objects to the Lyman break galaxies at  $z > 3$  observed in [O III] by Teplitz et al. (2000), most with narrowband filters in preselected  $z$  ranges. We constructed hybrid equivalent widths for [O III]  $\lambda 5007$ —from their spectroscopic fluxes and imaging broadband magnitudes—in the emitted frame. Their sample is more luminous in the 5000 Å continuum than ours, as might be expected from the selection methods. We can compare this spectral region directly between the two samples, since it falls in the *K* band for  $z = 3.3$  and the *H* or NICMOS F160W band at  $z = 2.4$ . Lack of detected H $\beta$  coupled with the observed [O III] strengths lead Teplitz et al. to infer [O/H] = 0.2–0.9 times solar for their objects, concluding that “most LBGs appear likely to have less than solar metallicity, and yet not to lie in the extremely low *Z* regime seen in low-mass local galaxies.” We argue that the less luminous and bluer Ly $\alpha$  emitters do extend into this regime. Their 5000 Å luminosities, averaged logarithmically, are typically about 3 times lower than the Lyman break systems, before any differential reddening correction (which would only increase this difference). Furthermore, we see evidence for a luminosity-metallicity connection within our sample, since the bluest objects are also the faintest in the emitted ultraviolet, as seen in Figure 5. We might speculate that either the more luminous objects began star formation earlier or that they have deeper potential wells and therefore can self-

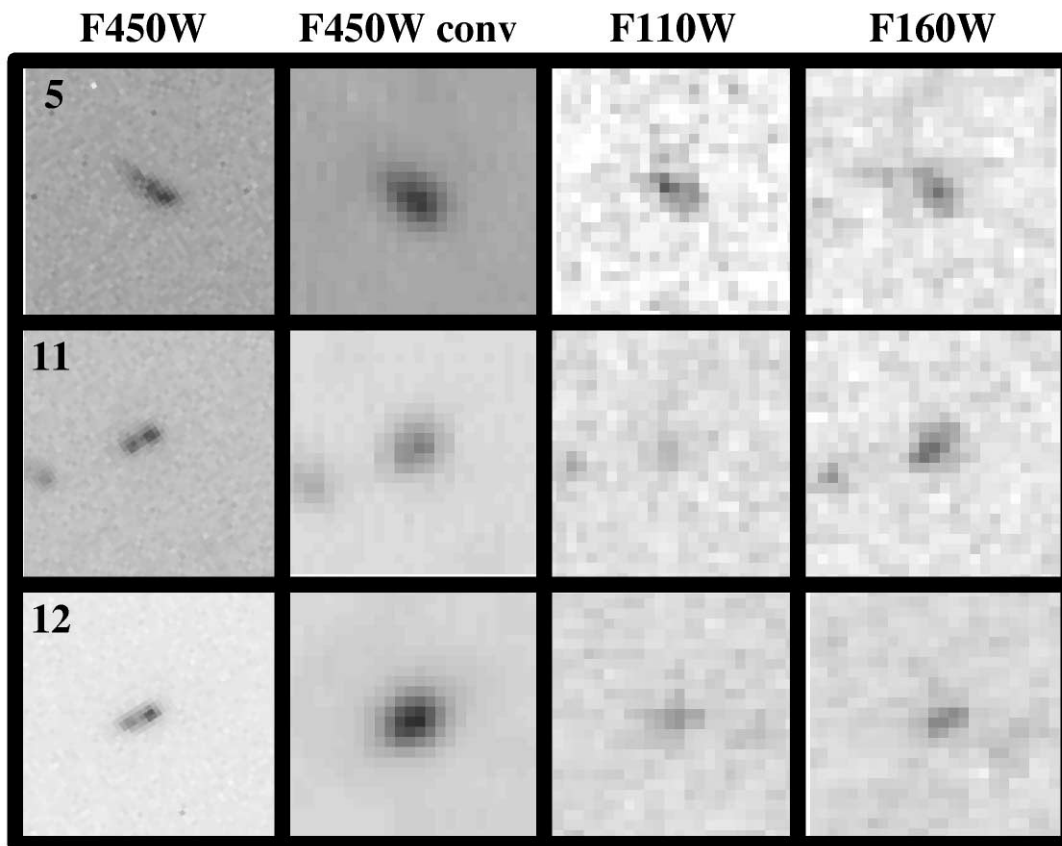


FIG. 9.—High-redshift objects that appear as close doubles in optical images. The  $B$  images are shown both in the original (WF interleaved or PC)  $0''.045$  pixel scale and after resampling and convolution to match the F160W PSF, as well as with the corresponding regions in the drizzled F110W and F160W images with  $0''.1$  pixels. Each region is  $2''.5$  on a side, aligned with the NICMOS detector coordinates so that north is roughly to the right (as depicted in Fig. 1). Consistency of the image centroids indicates that the color of the two components must in each case be similar across the  $0.4\text{--}1.6\ \mu\text{m}$  range.

enrich their gas supply more efficiently than the less luminous, presumably lower mass objects we see at  $z = 2.4$ .

Comparing this set of AGNs and star-forming objects in a narrow redshift range gives some hints on how AGN hosts and other systems differ at this epoch. The AGNs are interacting with their surroundings, as shown by structures that may be reflection and ionization cones. These are extensive enough to suggest material ejected from the AGN hosts, driven either by the AGNs themselves or by associated star formation. In either case, abundances in these winds, which are strong [O III] sources, as well as Ly $\alpha$  sources, are likely to be several times higher than in the star-forming objects, suggesting that star formation began earlier and perhaps at a higher rate in the AGN hosts. In contrast, the abundances in the fainter objects with active star formation are substantially below solar, so that either they have only recently begun star formation or have such shallow potential wells that they do not self-enrich. Either case poses interesting questions for the number density and fate of these objects—if they have been forming stars for only a few times  $10^7$  yr, why do we see so many of them? On the other hand, if they are losing material so rapidly, they should fade by a large factor unless replenished by infalling gas against the trend of mass loss driven by star formation. Multiple episodes of infall, star formation, and outflow might be needed if these objects are the precursors of luminous present-day galaxies.

If these systems are indeed losing their ISM by global winds, star formation will shut down quickly, and they will

fade passively. From the Bruzual & Charlot (1993) models, such passive evolution will amount to about 4–6 mag in  $V$ , depending on just how long the initial burst lasts. That would give these objects present-epoch  $V$  luminosities of order  $2 \times 10^{37}$  to  $5 \times 10^{38}$  ergs  $\text{s}^{-1} \text{\AA}^{-1}$  for absolute magnitudes  $M_V = -14$  to  $-17$ , respectable values for current gas-poor dwarf galaxies. It is therefore possible that in these systems we are observing an epoch of sweeping driven by starbursts, as described by Wyse & Silk (1985) and related to the nearby systems observed by Marlowe et al. (1995). By contrast, the AGNs may have hosted multiple or very protracted bursts of star formation, while the subgalactic objects have undergone fewer bursts, resulting in lower O/H, and perhaps winds that are overall less energetic (though still sufficient to escape their shallower potential wells).

Taken together, these results make sense in a broad hierarchical scheme, with the AGNs forming in those systems that started from the strongest fluctuations, collapsed first, and underwent the earliest star formation, leaving the lower mass objects to collapse later, perhaps undergoing their first widespread star formation near the observed epoch at  $z = 2.4$ . However, the unresolved questions about the fate of the star-forming objects still make it difficult to tie these systems together with present-day galaxies.

This work was supported by NASA through STScI grants GO-07459.\*-96A. Luminosities of nearby star-forming systems were calculated using *IUE* data retrieved from

the MAST archive maintained at STScI. Ned Wright's World Wide Web calculator for cosmological quantities was a time-saver, particularly in comparing data on objects at higher redshifts. We acknowledge as well a useful conver-

sation with Eric Bell in comparing experience fitting the  $\beta$  slope in various ways. We thank the referee, Rodger Thompson, for comments that led to improvement in our analysis, as well as discussion.

## REFERENCES

- Bell, E. F., Gordon, K. G., Kennicutt, R. C., Jr., & Zaritsky, D. 2002, *ApJ*, 565, 994
- Bruzual A., G., & Charlot, S. 1993, *ApJ*, 405, 538
- Cairós, L. M., Caon, N., Vilchez, J. M., González-Pérez, J. N., & Muñoz-Tuñón, C. 2001, *ApJS*, 136, 393
- Calzetti, D., Kinney, A. L., & Storchi-Bergmann, T. 1994, *ApJ*, 429, 582
- Colley, W. N., Gnedin, O. Y., Ostriker, J. P., & Rhoads, J. P. 1997, *ApJ*, 488, 579
- Colley, W. N., Rhoads, J. E., Ostriker, J. P., & Spergel, D. N. 1996, *ApJ*, 473, L63
- Copetti, M. V. F., Pastoriza, M. G., & Dottori, H. A. 1986, *A&A*, 156, 111
- Costero, R., & Osterbrock, D. E. 1977, *ApJ*, 211, 675
- De Robertis, M. M., & Osterbrock, D. E. 1986, *PASP*, 98, 629
- Gardner, J. P., & Satyapal, S. 2000, *AJ*, 119, 2589
- Giavalisco, M., Koratkar, A., & Calzetti, D. 1996, *ApJ*, 466, 831
- Haarsma, D. B., Partridge, R. B., Windhorst, R. A., & Richards, E. A. 2000, *ApJ*, 544, 641
- Hamann, F., Korista, K. T., Ferland, G. J., Warner, C., & Baldwin, J. 2002, *ApJ*, 564, 592
- Hawarden, T. G., Leggett, S. K., Letawsky, M. B., Ballantyne, D. R., & Casali, M. M. 2001, *MNRAS*, 325, 563
- Izotov, Y. I., & Thuan, T. X. 1999, *ApJ*, 511, 639
- Jacoby, G. H., Hunter, D. A., & Christian, C. A. 1984, *ApJS*, 56, 257
- Keel, W. C. 2002, in preparation
- Keel, W. C., Cohen, S., Windhorst, R. A., & Waddington, I. 1999, *AJ*, 118, 2547
- Keel, W. C., & Windhorst, R. A. 1991, *ApJ*, 383, 135
- Kobulnicky, H. A. 1998, in *ASP Conf. Ser. 147, Abundance Profiles: Diagnostic Tools for Galaxy History*, ed. D. Friedli, M. Edmunds, C. Robert, & L. Drissen (San Francisco: ASP), 108
- Lanzetta, K. M., Yahata, N., Pascarelle, S., Chen, H.-W., & Fernandez-Soto, A. 2002, *ApJ*, 570, in press
- Loose, H. H., & Thuan, T. X. 1986, in *Star-Forming Galaxies and Related Objects*, ed. D. Kunth, T. X. Thuan, & J. Trân Thanh Vân (Gif-sur-Yvette: Editions Frontières), 73
- Madau, P., Ferguson, H. C., Dickinson, M. E., Giavalisco, M., Steidel, C. C., & Fruchter, A. 1996, *MNRAS*, 283, 1388
- Madau, P., Pozzetti, L., & Dickinson, M. 1998, *ApJ*, 498, 106
- Marleau, F. R., & Simard, L. 1998, *ApJ*, 507, 585
- Marlowe, A. T., Heckman, T. M., Wyse, R. F. G., & Schommer, R. 1995, *ApJ*, 438, 563
- McQuade, K., Calzetti, D., & Kinney, A. L. 1995, *ApJS*, 97, 331
- Meurer, G. R., Heckman, T. M., & Calzetti, D. 1999, *ApJ*, 521, 64
- Mobasher, B., Rowan-Robinson, M., Georgakakis, A., & Eaton, N. 1996, *MNRAS*, 282, L7
- Motohara, K., et al. 2001, *PASJ*, 53, 459
- Osterbrock, D. E., & Miller, J. S. 1975, *ApJ*, 197, 535
- Owen, F. N., O'Dea, C. P., & Keel, W. C. 1990, *ApJ*, 352, 44
- Pagel, B. E. J., Edmunds, M. G., Blackwell, D. E., Chun, M. S., & Smith, G. 1979, *MNRAS*, 189, 95
- Pascarelle, S. M., Armus, L., Scoville, N. Z., Windhorst, R. A., & Cohen, S. H. 2002, *ApJ*, submitted
- Pascarelle, S. M., Lanzetta, K. M., & Fernandez-Soto, A. 1998a, *ApJ*, 508, L1
- Pascarelle, S. M., Windhorst, R. A., & Keel, W. C. 1998b, *AJ*, 116, 2659 (P98)
- Pascarelle, S. M., Windhorst, R. A., Keel, W. C., & Odewahn, S. C. 1996, *Nature*, 383, 45 (P96)
- Pettini, M., Shapley, A. E., Steidel, C. C., Cuby, J.-G., Dickinson, M., Moorwood, A. F. M., Adelberger, K. L., & Giavalisco, M. 2001, *ApJ*, 554, 981
- Schulte-Ladbeck, R. E., Hopp, U., Crone, M. M., & Greggio, L. 1999a, *ApJ*, 525, 709
- Schulte-Ladbeck, R. E., Hopp, U., Greggio, L., & Crone, M. M. 1999b, *AJ*, 118, 2705
- Stasinska, G., & Leitherer, C. 1996, *ApJS*, 107, 661
- Teplitz, H. I., et al. 2000, *ApJ*, 542, 18
- Thompson, R. I., Weymann, R. J., & Storrie-Lombardi, L. J. 2001, *ApJ*, 546, 694
- Tripp, T. B., Savage, B. D., & Jenkins, E. B. 2000, *ApJ*, 534, L1
- Windhorst, R. A., et al. 1991, *ApJ*, 380, 362
- Windhorst, R. A., Gordon, J. M., Pascarelle, S. M., Schmidtke, P. C., Keel, W. C., Burkey, J. M., & Dunlop, J. S. 1994, *ApJ*, 435, 577
- Windhorst, R. A., Keel, W. C., & Pascarelle, S. M. 1998, *ApJ*, 494, L27
- Wyse, R. F. G., & Silk, J. 1985, *ApJ*, 296, L1